

Edge gyrokinetic theory and continuum simulations

X.Q. Xu¹, Z. Xiong¹, M.R. Dorr¹, J.A. Hittinger¹, K. Bodi², J. Candy³, B.I. Cohen¹, R.H. Cohen¹, P. Colella⁴, G.D. Kerbel¹, S. Krasheninnikov², W.M. Nevins¹, H. Qin⁵, T.D. Rognlien¹, P.B. Snyder³ and M.V. Umansky¹

¹ Lawrence Livermore National Laboratory, Livermore, CA 94551, USA

² University of California, San Diego, La Jolla, CA 92093, USA

³ General Atomics, San Diego, CA 92186, USA

⁴ Lawrence Berkeley National Laboratory, Berkeley, CA 94720, USA

⁵ Princeton Plasma Physics Laboratory, Princeton, NJ 08543, USA

E-mail: xxu@llnl.gov

Received 10 January 2007, accepted for publication 21 May 2007

Published 23 July 2007

Online at stacks.iop.org/NF/47/809

Abstract

The following results are presented from the development and application of TEMPEST, a fully nonlinear (full-f) five-dimensional (3d2v) gyrokinetic continuum edge-plasma code. (1) As a test of the interaction of collisions and parallel streaming, TEMPEST is compared with published analytic and numerical results for endloss of particles confined by combined electrostatic and magnetic wells. Good agreement is found over a wide range of collisionality, confining potential and mirror ratio, and the required velocity space resolution is modest. (2) In a large-aspect-ratio circular geometry, excellent agreement is found for a neoclassical equilibrium with parallel ion flow in the banana regime with zero temperature gradient and radial electric field. (3) The four-dimensional (2d2v) version of the code produces the first self-consistent simulation results of collisionless damping of geodesic acoustic modes and zonal flow (Rosenbluth–Hinton residual) with Boltzmann electrons using a full-f code. The electric field is also found to agree with the standard neoclassical expression for steep density and ion temperature gradients in the plateau regime. In divertor geometry, it is found that the endloss of particles and energy induces parallel flow stronger than the core neoclassical predictions in the SOL.

PACS numbers: 52.25.Fi, 52.35.Ra, 52.40.Kh, 52.55.Fa, 52.65.Tt

1. Introduction

Understanding the structure of the edge transport barrier in high-performance (H-mode) discharges requires a kinetic description of the plasmas because the radial width of the pedestal observed in experiments is comparable to the radial width of individual ion drift orbits (leading to a large distortion of the local distribution function from a Maxwellian), and because the ion and electron mean-free-paths are long compared with the connection length for the hot plasma at the top of the edge pedestal (violating the assumptions underlying collisional fluid models). A gyrokinetic formulation (2v) [1] is a reasonable approximation for edge plasmas because it is believed that pedestal physics is likely dominated by phenomena having low frequencies compared with the ion gyrofrequency. But previous gyrokinetic theories and codes do not apply to edge plasmas because they cannot treat fully nonlinear (full-f) electromagnetic perturbations with

multi-scale-length structures in space–time for full divertor geometry.

We report on the development and application of TEMPEST, a full-f gyrokinetic code, to simulate H-mode edge plasmas. This five-dimensional ($\psi, \theta, \zeta, E_0, \mu$) continuum code represents velocity space via a grid in equilibrium energy (E_0) and magnetic moment (μ) variables and configuration space via a grid in poloidal magnetic flux (ψ), poloidal angle (θ) and toroidal angle (ζ). The geometry can be a circular annulus or that of a diverted tokamak and so includes boundary conditions for both closed magnetic flux surfaces and open field lines. The same set of gyrokinetic equations [2, 3] is discretized for both geometries. The equations are solved via a method-of-lines approach and an implicit backward-differencing scheme using a Newton–Krylov iteration to advance the system in time [4]. The spatial derivatives are discretized with finite differences while a high-order finite-volume method is used in velocity space (E_0, μ).

A fourth-order upwinding algorithm is used for parallel streaming, and a fifth-order WENO scheme [5] is used for particle cross-field drifts. Boundary conditions at conducting material surfaces are implemented on the plasma side of the sheath. The code includes kinetic or Boltzmann electrons. A nonlinear Fokker–Planck collision operator (CQL) from the STELLA code [6] has been extracted and integrated into TEMPEST using the same implicit Newton–Krylov solver. A new Fokker–Planck collision operator in (E_0, μ) space is under development for improved accuracy and conservation properties [7]. The gyrokinetic Poisson (GKP) equation is solved self-consistently with the gyrokinetic equations as a differential-algebraic system involving a nonlinear system solve via a Newton–Krylov iteration using a multigrid preconditioned conjugate gradient (PCG) solver for the Poisson equation.

2. Basic gyrokinetic equation

A set of generalized gyrokinetic Vlasov–Maxwell equations valid for edge-plasma conditions has been derived in the gyrocentre coordinate system by the Lie transform perturbation method, which uses the Poincaré–Cartan–Einstein 1-form and the pullback transformation for the distribution function [2]. This formalism allows inclusion of nonlinear large-amplitude, time-dependent background electromagnetic fields in addition to small-amplitude, short-wavelength electromagnetic perturbations. As an example, the pullback transformation in the GKP equation is explicitly expressed in terms of moments of the gyrocentre distribution function, thus describing the important gyro-orbit squeezing effect due to the large electric field gradients in the edge and the full finite Larmor radius effect for short-wavelength fluctuations. The familiar polarization-drift density in the gyrocentre Poisson equation is replaced by a more general expression.

2.1. Full- f electrostatic ion gyrokinetic equations

The electrostatic ion gyrokinetic equations presently implemented in TEMPEST for the time-dependent five-dimensional (5D) distribution functions are simplified from our recent new formulation [2] and Hahm’s earlier work [3]. In order to accurately simulate particle parallel streaming, the large electrostatic potential Φ , which has multiple spatial-time scales, is split into two parts $\Phi = \Phi_0 + \delta\phi$: Φ_0 is the large-amplitude, slowly varying component; $\delta\phi$ is the small-amplitude, rapidly varying component. Here E_0 is defined as the total energy including Φ_0 , but not $\delta\phi$. Then E_0 is a constant of motion if $\delta\phi \sim 0$ and $\partial\langle\Phi_0\rangle/\partial t \sim 0$ for a coordinate aligned with the direction of phase-space flow. The kinetic equation for the gyrocentre distribution function $F_\alpha(\bar{\mathbf{x}}, \bar{\mu}, \bar{E}_0, t)$ in gyrocentre coordinates ($\bar{\mathbf{x}} = \mathbf{x} - \rho_\alpha$, $\rho_\alpha = \mathbf{b} \times \mathbf{v}/\Omega_{c\alpha}$), ‘equilibrium energy’ \bar{E}_0 and magnetic moment $\bar{\mu}$ has the form

$$\frac{\partial F_\alpha}{\partial t} + \bar{\mathbf{v}}_d \cdot \frac{\partial F_\alpha}{\partial \bar{\mathbf{x}}_\perp} + (\bar{v}_\parallel + \bar{v}_{\text{Banos}}) \mathbf{b} \cdot \frac{\partial F_\alpha}{\partial \bar{\mathbf{x}}} + \left[q \frac{\partial \langle \Phi_0 \rangle}{\partial t} + \bar{\mu} \frac{\partial B}{\partial t} - \frac{B}{B_\parallel^*} \bar{v}_\parallel q \frac{\partial \langle \delta\phi \rangle}{\partial s} - \mathbf{v}_{d0} \cdot (q \bar{\nabla} \langle \delta\phi \rangle) \right] \frac{\partial F_\alpha}{\partial E_0} = C(F_\alpha, F_\alpha), \quad (1)$$

$$\bar{\mathbf{v}}_d = \frac{c\mathbf{b}}{qB_\parallel^*} \times (q\bar{\nabla} \langle \Phi \rangle + \bar{\mu} \bar{\nabla} B) + \bar{v}_\parallel^2 \frac{M_\alpha c}{qB_\parallel^*} (\bar{\nabla} \times \mathbf{b}), \quad (2)$$

$$\bar{\mathbf{v}}_{d0} = \frac{c\mathbf{b}}{qB_\parallel^*} \times (q\bar{\nabla} \langle \Phi_0 \rangle + \bar{\mu} \bar{\nabla} B) + \bar{v}_\parallel^2 \frac{M_\alpha c}{qB_\parallel^*} (\bar{\nabla} \times \mathbf{b}), \quad (3)$$

$$\bar{v}_\parallel = \pm \sqrt{\frac{2}{M_\alpha} (E_0 - \bar{\mu} B - q \langle \Phi_0 \rangle)},$$

$$v_{\text{Banos}} = \frac{\mu c}{q} (\mathbf{b} \cdot \bar{\nabla} \times \mathbf{b}), \quad (4)$$

$$B_\parallel^* \equiv B \left[1 + \frac{\mathbf{b}}{\Omega_{c\alpha}} \cdot (v_\parallel \bar{\nabla} \times \mathbf{b}) \right], \quad \Omega_{c\alpha} = \frac{qB}{M_\alpha c},$$

$$\mu = \frac{M_\alpha v_\perp^2}{2B}, \quad (5)$$

$$\langle \delta\phi \rangle = \langle \Phi \rangle - \langle \Phi_0 \rangle. \quad (6)$$

Here $q = Z_\alpha e$, M_α are the electric charge and the mass of electrons ($\alpha = e$) and ions ($\alpha = i$). The left-hand side of equation (1) describes particle motion in electric and magnetic fields. C_α is the Coulomb collision operator. The overbar is used for the gyrocentre variables and $\langle \rangle$ denotes the gyroangle averaging. Additional $\mathbf{E}_0 \times \mathbf{B}$ flow terms due to the large amplitude and slow variation of Φ_0 from the complete formulation [2] will be added.

2.2. Full- f GKP equation

The complete GKP equation has been recently derived in (a) of [2], including orbit squeezing by large E_r shearing and full FLR effect. To make it numerically tractable, two additional approximations are made here: (1) the spatial variation of the transverse $\bar{\mu}$ moments $M_n(\bar{\mathbf{x}})$ calculated from $F_\alpha(\bar{\mathbf{x}}, \bar{\mu}, \bar{E}_0, t)$ is assumed much slower than that of the potential in evaluating the full FLR effect; (2) the total transverse distribution function is Maxwellian with temperature $T_{\perp\alpha}$.

2.2.1. Full- f GKP equation in the arbitrary wavelength regime. In the arbitrary wavelength regime, the self-consistent electrostatic potential is computed from the GKP equation:

$$0 = -4\pi e \left[\sum_\alpha Z_\alpha N_\alpha(\mathbf{x}, t) - n_e(\mathbf{x}, t) \right] - \sum_\alpha \frac{1}{\lambda_{D\alpha}^2} [\Gamma_0(b) - 1] \Phi, \quad (7)$$

where $\Gamma_0(b) = I_0(b)e^{-b}$, $b = \rho_\alpha^2 \nabla_\perp^2 / 2$ and $I_0(b)$ is the usual zeroth-order modified Bessel function. The ion gyroradius is $\rho_\alpha = \sqrt{2T_{\perp\alpha}/M_\alpha}/\Omega_\alpha$, the ion gyrofrequency is $\Omega_\alpha = Z_\alpha e B / M_\alpha c$ and the ion Debye length is $\lambda_{D\alpha}^2 = T_{\perp\alpha} / 4\pi N_\alpha Z_\alpha^2 e^2$. Although equation (7) is similar to the usual GKP equation [3], there is an important distinction. Our GKP equation is full- f and the gyrocentre density N_α and perpendicular ion pressure $p_{\perp\alpha}$ are calculated from the gyrocentre distribution function $F_\alpha(\bar{\mathbf{x}}, \bar{\mu}, \bar{E}_0, t)$.

$$N_\alpha(\mathbf{x}, t) \equiv \frac{2\pi}{M_\alpha} \int B_\parallel^* d\bar{v}_\parallel d\bar{\mu} F_\alpha, \quad (8)$$

$$n_e(\mathbf{x}, t) \equiv \frac{2\pi}{m_e} \int B_\parallel^* dv_\parallel d\mu f_e,$$

$$p_{\perp\alpha} = \pi B \int dv_\parallel d\bar{\mu} (v_\perp^2 F_\alpha), \quad T_{\perp\alpha} = \frac{p_{\perp\alpha}}{N_\alpha(\mathbf{x}, t)}. \quad (9)$$

Here the dot product between the density gradient vector and potential gradient vector, as well as the Debye shielding, have been dropped for simplicity in equation (7).

The first-order Padé approximation to Γ_0 , $\Gamma_0 - 1 = b/(1 + b)$, is an excellent fit for $0 \leq b \leq 9$ and is therefore valid well into the typical ion gyrokinetic regime as shown previously in gyrokinetic and gyrofluid simulations [8, 9]. Substituting a simple functional transformation $\Phi = \phi_L + [T_{\perp\alpha}/(N_\alpha Z_\alpha^2 e)][Z_\alpha N_\alpha(\mathbf{x}, t) - n_e(\mathbf{x}, t)]$ and the Padé approximation into equation (7) yields

$$\frac{\rho_\alpha^2}{2} \nabla_\perp^2 \phi_L = -\frac{T_\alpha}{N_\alpha Z_\alpha^2 e} [Z_\alpha N_\alpha(\mathbf{x}, t) - n_e(\mathbf{x}, t)]. \quad (10)$$

where ϕ_L is calculated by the GKP solver.

2.2.2. Full-f GKP equation in the long wavelength regime. In the long wavelength limit $k_\perp \rho_\alpha \ll 1$, the self-consistent electric field is typically computed from the GKP equation for multiple species:

$$\sum_\alpha \frac{\rho_\alpha^2}{2\lambda_{D\alpha}^2} \nabla_\perp \cdot (\ln N_\alpha \nabla_\perp \Phi) + \nabla^2 \Phi = -4\pi e \left[\sum_\alpha Z_\alpha N_\alpha(\mathbf{x}, t) - n_e(\mathbf{x}, t) \right] - \sum_\alpha \frac{\rho_\alpha^2}{2\lambda_{D\alpha}^2} \frac{1}{N_\alpha Z_\alpha e} \nabla_\perp^2 p_{\perp\alpha}. \quad (11)$$

In the long wavelength regime, the approximation $\nabla N_\alpha \ll \nabla \Phi$ is not used. There are two important distinctions between equation (11) and the usual GKP equation [3]. Our GKP equation is full-f with the gyrocentre density N_α and perpendicular ion pressure $p_{\perp\alpha}$ calculated from the gyrocentre distribution function $F_\alpha(\bar{\mathbf{x}}, \bar{\mu}, \bar{E}_0, t)$ defined in equations (8) and (9). The last term of equation (11) is the diamagnetic density from the long wavelength expansion of the gyroaveraged gyrocentre density $N_\alpha(\mathbf{x}, t)$, i.e. from the pullback transform. Although the diamagnetic density is small compared with the ion gyrocentre density, it is of the same order as both the polarization density in high-beta plasmas and the difference between ion and electron gyrocentre densities. This equation is an extension of the typical neoclassical electric field model including poloidal variation [10].

2.3. Boundary conditions

2.3.1. Radial boundary conditions. Radial Robin boundary conditions are used for F_α and potential Φ at the inner core surface $\psi = \psi_c$ and the outer wall surface $\psi = \psi_w$. Robin boundary conditions consist of specification of a linear combination of a field value and its normal derivative at all points of the boundary surface $\psi = \psi_{c,w}$, such as $\alpha_b \Phi^b + \beta_b \partial \Phi^b / \partial \psi$, where α_b , β_b , Φ^b and $\partial \Phi^b / \partial \psi$ are prescribed. This is a generalization of Dirichlet ($\alpha_b = 1$ and $\beta_b = 0$) and Neumann ($\alpha_b = 0$ and $\beta_b = 1$) boundary conditions. Since the gyrokinetic equation has only a first-order radial advection term, only one boundary condition is used and then only where the convection is into the domain. No boundary condition should be imposed for particles convecting out of the domain; therefore an extrapolation is used at that boundary.

2.3.2. Poloidal boundary conditions. The boundary conditions in the θ direction for F_α and for Φ are sheath boundary conditions at the divertor plates, and a twist-shifted (in 5D) parallel periodic condition in the ‘‘core’’ for field-line-aligned coordinates [11–13]. Our present implementation for sheath boundary conditions consists of absorption of all ions incident at the wall in the absence of biasing, and absorption of electrons energetic enough to escape the sheath potential and reach the wall, i.e. $E_0 = e\delta\phi_{sh} - \mu B > 0$. Here $\Phi_{sh} = \Phi_{0sh} + \delta\phi_{sh}$ is the sheath potential. Optionally, a fraction of escaping ions and electrons can be reflected.

2.3.2.1. Sheath boundary conditions for potential. If the gyrokinetic ion and fluid electron model are used, the sheath potential is determined by the ambipolarity condition:

$$\Phi_{sh} = \frac{T_{e,sh}}{e} \ln \left[\frac{4\Gamma_{i,sh}}{n_{e,sh}\zeta\sqrt{8T_{e,sh}/\pi m_e}} \right], \quad (12)$$

$$\Gamma_{i,sh} = \frac{2\pi B}{M_i^2} \int_{q\Phi_{0sh}}^\infty dE_0 \int_0^{(E_0 - q\Phi_{0sh})/B} \frac{d\mu}{|v_\parallel|} v_\parallel F_i^\sigma.$$

The $\sigma = \pm$ represents the plus and minus sheets of parallel velocity with $F_i^\sigma \neq 0$ for only the incoming particle sheet. Here it is assumed that impinging electrons have a Maxwellian distribution. The factor $\zeta \equiv 1/(1 + \tau_p/\tau_e)$ includes a correction for electron long mean-free path physics. τ_p is long mean-free path confinement time and τ_e is the confinement time for the collisional sheath-limited case. $\zeta \equiv 1$ if the electrons are in the short mean-free path regime. The $n_{e,sh}$ and $T_{e,sh}$ are the electron density and temperature on the plasma side of the sheath.

If both electrons and ions are kinetic, the sheath potential is determined by the quasi-neutrality condition at the sheath entrance:

$$\Gamma_{i,sh} = \frac{2\pi B}{M_i^2} \int_{q\Phi_{0sh}}^\infty dE_0 \int_0^{(E_0 - q\Phi_{0sh})/B} \frac{d\mu}{|v_\parallel|} v_\parallel F_i^\sigma, \quad (13)$$

$$\Gamma_{e,sh} = \frac{2\pi B}{m_e^2} \int_{e\delta\phi_{sh}}^\infty dE_0 \int_0^{(E_0 - e\delta\phi_{sh})/B} \frac{d\mu}{|v_\parallel|} v_\parallel F_e^\sigma,$$

$$\Gamma_{i,sh} \simeq \Gamma_{e,sh}, \quad (14)$$

where there is an energetic group of impinging electrons that overcome the potential barrier and reach the wall with the energy $E_0 > \mu B - e\delta\phi_{sh}$.

2.3.2.2. Sheath boundary conditions for distribution functions. If the gyrokinetic ion and fluid electron model is used, the ion distribution function is:

$$F_\alpha(\psi, \theta, E_0, \mu) = \begin{cases} F_\alpha(\psi, \theta, E_0, \mu), & v_\parallel \geq 0, \\ 0, & v_\parallel \leq 0. \end{cases} \quad (15)$$

A convention regarding the sign of the parallel velocity is that it is positive when it points in the direction of increasing θ . Here θ increases towards the outer divertor plate.

If both electrons and ions are kinetic, the electron distribution function is

$$f_e(\psi, \theta, E_0, \mu, \sigma = -1) = \begin{cases} f_e(\psi, \theta, E_0, \mu, \sigma = 1), & |v_\parallel| \leq v_{sh}, \\ 0, & |v_\parallel| \geq v_{sh}. \end{cases} \quad (16)$$

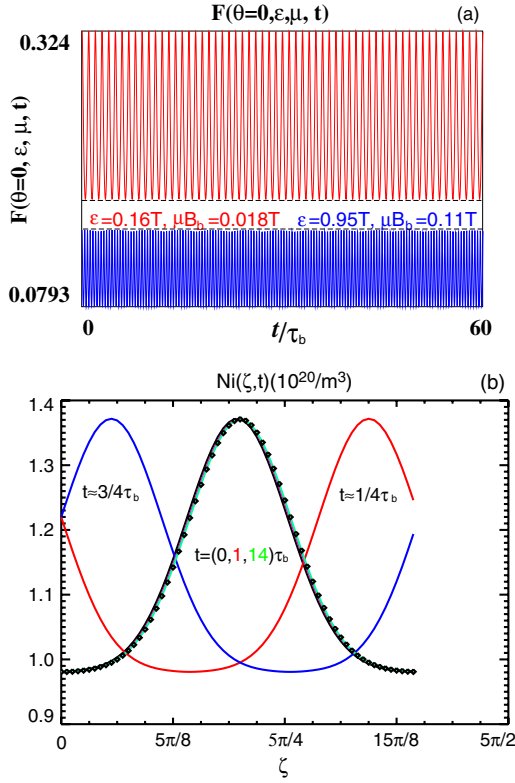


Figure 1. (a) Time evolution of the distribution function for circulating particles using a fourth-order upwinding scheme. The equilibrium electrostatic potential $\Phi_0 = 0.0$, $\epsilon = a/R_0 = 0.3$, the minor radius $a = 0.51$ m, $Z_\alpha = 1$, poloidal magnetic field $B_p = 0.3$ T. (b) The density versus toroidal angle at different times for toroidal convection using a fifth order Weno scheme. The ion transit time τ_b is defined as $\tau_b = R/v_{Ti}$, $v_{Ti} = \sqrt{2T_i/M_i}$.

Here $v_{sh} = \sqrt{2e\Phi_{sh}/m_e}$ is the electron threshold velocity determined by the sheath potential Φ_{sh} .

3. TEMPEST simulation schemes

The TEMPEST gyrokinetic equations and GKP equation are self-consistently integrated as a differential-algebraic system involving a nonlinear system solve via Newton–Krylov iteration. The spatial derivatives are discretized with finite differences while a high-order finite-volume method is used in velocity space (E_0, μ). A fourth-order upwinding algorithm is used for parallel streaming, and a fifth-order WENO scheme [5] is used for particle cross-field drifts. The GKP equation, the drift velocities and acceleration are discretized using centred differencing. Boundary conditions at conducting material surfaces are implemented on the plasma side of the sheath. The GKP preconditioner block is inverted using a multigrid PCG solver. The PCG solver and preconditioners are provided by the Hypr library using the “semi-structured interface” [14]. The code includes kinetic or Boltzmann electrons. The Boltzmann relation in the adiabatic option employs flux surface averaging to maintain neutrality within field lines and is solved self-consistently with the GKP equation. A decomposition procedure circumvents the near singularity of the GKP Jacobian block that otherwise degrades CG convergence.

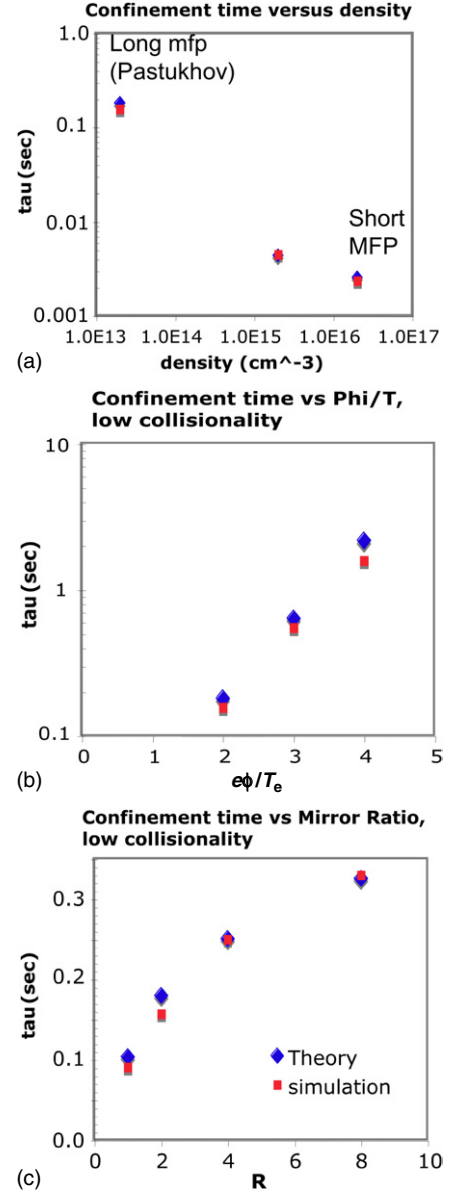


Figure 2. Collisional endloss (“Pastukhov”) test cases: (a) confinement time versus density; (b) confinement time versus potential $e\phi/T_e$ at low collisionality; (c) confinement versus mirror ratio at low collisionality.

TEMPEST uses a Python scripting front end that allows the gyrokinetic code to interface with other codes, such as the edge transport code UEDGE and other physics packages, implemented as Python modules. We have designed and implemented flexible C++ data structures for the management of distributed arrays and supporting data objects on top of the structured adaptive mesh refinement application infrastructure (SAMRAI) [15] and Chombo [16]. The data layout is defined on distributed and disjoint unions of rectangular blocks, but with arbitrary interblock connectivity (nonlocal communication) for multiple regions in the edge plasma across the magnetic separatrix.

The gyrokinetic equation is primarily particle convection both in configuration and velocity spaces. An accurate, stable and weakly damped convection scheme is extremely important

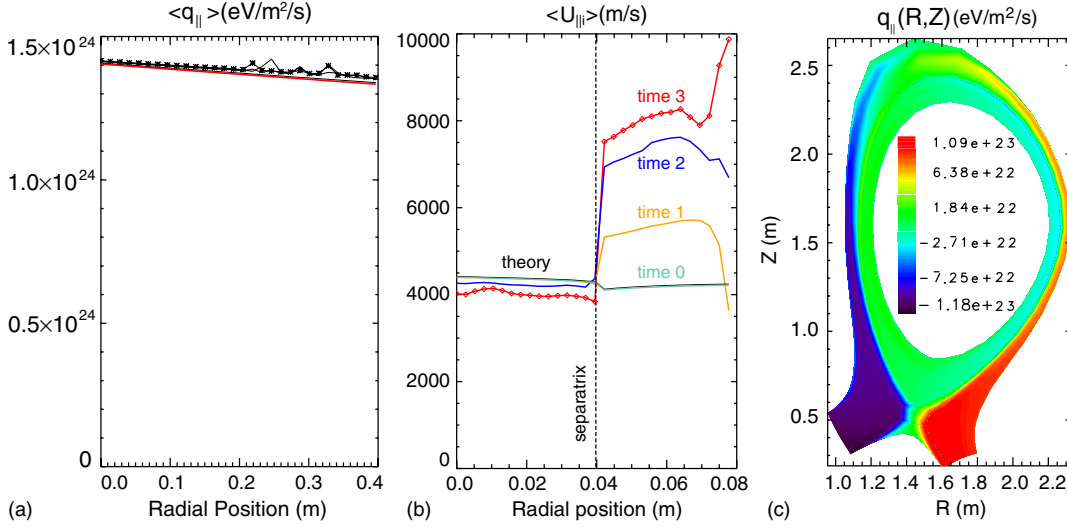


Figure 3. (a) Comparison between simulation results with theory (red solid line) for a collisionless case with $\nabla T_i = 0$ and zero finite banana-orbit width. Flux surface averaged parallel heat flux $\langle q_{\parallel} \rangle$. The red solid line is from theory $q_{\parallel\alpha} = 2.5N_{\alpha}U_{\parallel\alpha}T_{\alpha}$ and the other lines are from simulation results at different times after 10 thermal ion transit times; (b) comparison of simulation results with theory for flux surface averaged parallel flow velocity $\langle U_{\parallel} \rangle$ in the banana regime with $\nu_{*i} \simeq 0.02$, $\nabla T_i = 0$ and finite banana-orbit width in X-point divertor geometry. The average is done by integration along the field line from the inner plate to the outer plate in the SOL. (c) The contours of parallel heat flux $q_{\parallel}(R, Z)$ in the divertor geometry.

for the success of continuum gyrokinetic simulations. Here we present tests of our convection scheme for parallel streaming and toroidal drift. The fourth-order upwind scheme for parallel streaming is given in the appendix. The complete description and tests of the code algorithms will be given in a future publication.

3.1. Parallel streaming

The streaming test is done in a circular geometry with magnetic field $B(\theta) = B_0/(1 + \epsilon \cos \theta)$, $\epsilon = a/R_0 = 0.3$, the minor radius $a = 0.51$ m and poloidal magnetic field $B_p = 0.3$ T. The range of the variables: $0 \leq \theta \leq 2\pi$, $0 \leq v_{\parallel} \leq 3v_{th}$. The initial distribution function is $F_0 = (B_0/B)F_M$, where F_M is a Maxwellian distribution. For a given energy E_0 and magnetic moment μ in velocity space, F_0 has a peaked profile in the θ -coordinate due to $B(\theta)$. As the time evolves, the pulse will propagate along the magnetic field due to the parallel streaming. In the absence of the toroidal direction for 4D TEMPEST, the field line is closed and the pulse should periodically propagate along the poloidal angle θ . The oscillations at a specified poloidal position θ for a given energy E_0 and μ in velocity space represent the convection along the particle trajectory for the closed magnetic field line. For an ideal numerical difference scheme for convection, the amplitude should exhibit regular oscillations in time around a constant mean. The time evolution of the distribution function is plotted in figure 1(a), which shows an almost ideal oscillation for the expected periods of a circulating particle far away from the trapping–untrapping boundary using the fourth-order upwinding scheme given in the appendix. For a second-order upwinding scheme, a slight downward drift is observed; while for the third-order upwinding scheme, a small amount of damping is observed. However, even with the fourth-order upwinding scheme, the damping is strong for barely circulating particles and barely trapped particles due to nonuniform (orbit

time τ) grid spacing (not shown), $d\tau = \int_{l_i}^{l_{i+1}} dl/v_{\parallel}$ and dl is the arc length of a magnetic field line.

3.2. Toroidal convection

A similar test has been done for a toroidal drift using a fifth-order Weno scheme. Figure 1(b) shows the density versus toroidal angle for different times. An initial pulse is prescribed, centred at the middle of the toroidal simulation domain. As the time evolves, the pulse propagates due to the toroidal drift and should come back to its initial position with the same shape due to toroidal periodicity. A good numerical scheme should preserve this property. As we can see from figure 1(b), our scheme preserves the property very well after the 14 cycles. There is no significant damping or deformation from the original pulse. The primary reason for using the fifth-order Weno scheme is the existence of radial regions for particles with given energy E_0 and magnetic moment μ that are inaccessible under the influence of radial magnetic drifts.

4. TEMPEST simulation results

To facilitate verification and validation, both full-f and delta-f options are available for either circular or divertor geometry. TEMPEST is runnable as (1) 3D for parallel (to B) physics studies $F(\theta, E_0, \mu)$, (2) 4D for axisymmetric transport $F(\psi, \theta, E_0, \mu)$ and (3) 5D for turbulence $F(\psi, \theta, \zeta, E_0, \mu)$. The different aspects of 3D, 4D and 5D TEMPEST have been verified on various known physics problems: (1) collisional scattering into a velocity-space loss cone, (2) neoclassical flow and transport, (3) electric field generation and geodesic acoustic mode (GAM) damping and (4) self-consistent radial electric field for steep density and ion temperature gradients (ITGs). In addition, the initial runs have been done in 5D for drift waves and ITG modes (to be described elsewhere).

For the preliminary physics problems studied in this paper, the gyrokinetic Poisson equation (11) has been used without the diamagnetic density term and Φ_0 has been set to be zero for simplicity, except in section 4.1. In the future we will test the separation of the electrostatic potential into Φ_0 and $\delta\phi$.

4.1. 3D Pastukhov collisional endloss

As a test of collisional velocity space transport and parallel streaming, 3D TEMPEST (1d2v) simulation results are compared with published analytical and numerical results as shown in figure 2 for the endloss of particles confined by combined electrostatic and magnetic wells [17–19]. Here the electrostatic and magnetic fields are uniform in the simulation volume, with abrupt increases at the walls (incorporated into the boundary conditions). Good agreement is found over a wide range of collisionality, confining potential and mirror ratio; the required velocity space resolution is modest. In these simulations, the linearized CQL collision package is used.

4.2. 4D neoclassical flows

For a shifted Maxwellian distribution that analytically satisfies equation (1) for the zero finite banana-orbit size as an initial condition, TEMPEST should preserve the solution without any significant change (within our finite-difference truncation accuracy) after running some time steps. We tested such a case using the following simulation parameters: inverse aspect ratio $\epsilon = a/R_0 = 0.03$, the major radius $R_0 = 17.1$ m, toroidal magnetic field $B_t = 1.5$ T and poloidal magnetic field $B_p = 0.2$ T. The ion density profile is $n_i(\psi) = N_{ix} \exp(-\ln(N_{ix}/N_{io})\psi/L_\psi)$ with $N_{ix} = 1 \times 10^{20} \text{ m}^{-3}$ and $N_{io} = 0.95N_{ix}$. The ion temperature profile is flat with $T_i = 3$ keV. The mesh resolutions are $n_\psi = 30$, $n_\theta = 50$, $n_E = 60$ and $n_\mu = 30$. In the simulations Φ is set to zero for simplicity. As shown in figure 3(a), the simulation results remain in good agreement with theoretical prediction even after 10 000 time steps (~ 50 thermal ion transit times). The solid line in the plot of $q_{||i}$ comes from a theoretical prediction for a shifted Maxwellian distribution, $q_{||\alpha} = 2.5N_\alpha U_{||\alpha} T_\alpha$ and $U_{||\alpha} = -(I/\Omega_\alpha)(T_\alpha/M_\alpha)(\partial \ln N_\alpha/\partial \psi)$. The simulation curves cannot be differentiated, indicating that the system has reached a steady state solution.

In divertor geometry with given particle and heat sources on the inner core boundary surface and the ion density and temperature profiles $n_i(\psi) = N_{ix} \exp(-\ln(N_{ix}/N_{io})\psi/L_\psi)$, and $T_i(\psi) = T_{ix} \exp(-\ln(T_{ix}/T_{io})\psi/L_\psi)$ with $T_{ix} = 3$ keV, $T_{io} = 0.95T_{ix}$, $N_{ix} = 1 \times 10^{20} \text{ m}^{-3}$, and $N_{io} = 0.95N_{ix}$, it is found that the dominance of rapid parallel endloss of particles and energy in the SOL induces a parallel flow that is stronger than core neoclassical predictions in the SOL as indicated in figure 3(b); a symmetry point is developed for the parallel heat flux on the top of the machine as expected as shown in figure 3(c). For the temperature $T_e = T_i = 3$ keV and deuterium ion, the sound speed is $3.79 \times 10^5 \text{ m s}^{-1}$. Therefore the maximum March number for the flux surface averaged velocity is less than 0.025. Here the three different times are all at the initial transient on the order of ion transit time and the flow does not reach a steady state yet. The final steady state depends on the models of sources and sinks. The further comparison of the code results with other divertor codes is in progress and will be reported in a separate paper [20].

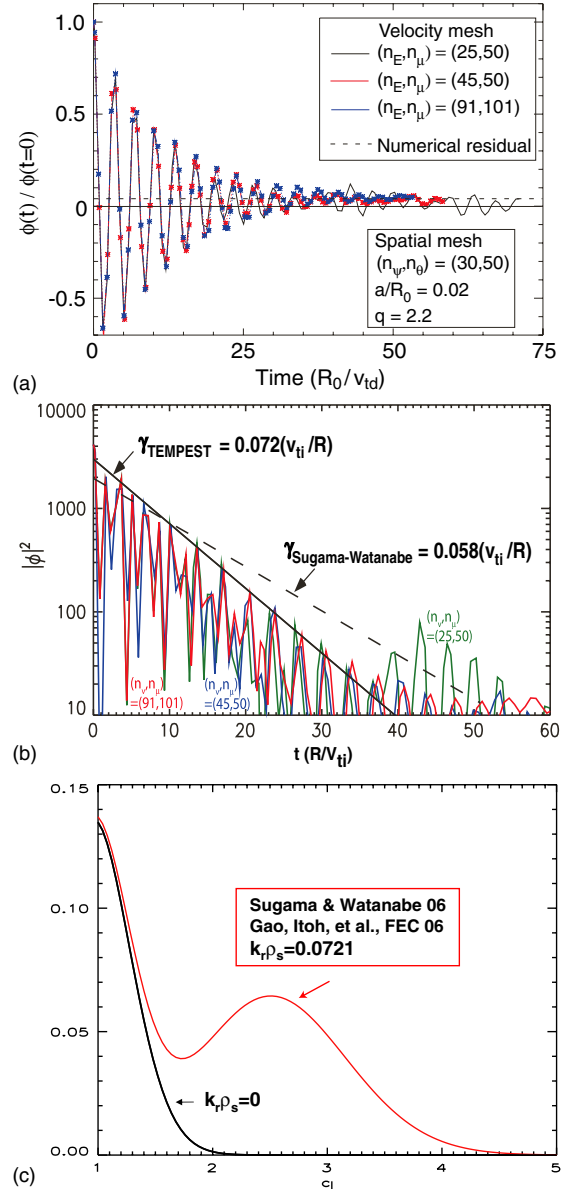


Figure 4. (a) Time evolution of the zonal-GAM potential shows GAM oscillation, collisionless damping and residual for a large-aspect-ratio circular geometry with $q = 2.2$ and $\epsilon = 0.02$ with three different velocity space resolutions; (b) comparison of simulation results for $|\phi|^2$ ($k_r \rho_s = 0.0721$, $\theta = 0$, t) with theory for the GAM damping rate at three different velocity resolutions in finite drift orbit regime; (c) GAM damping rate versus q with finite drift orbit effect (red) and without finite drift orbit effect (black) from Sugama and Watanabe theory [23].

4.3. 4D GAMs

The GAM is a poloidal asymmetric mode, which involves parallel ion dynamics, cross-field drifts and acceleration. Earlier GAM theory and simulations focused on the large-aspect-ratio, small orbit [21, 22] regime. Recently Sugama and Watanabe found that the damping rate is sensitive to $k_\perp \rho_i$ at large $q = \epsilon B_t/B_p$ due to the effect of large drift orbits [23]. In our 4D GAM simulations, the charge is radially separated by an initial sinusoidal perturbation of the ion density. The electron model is Boltzmann

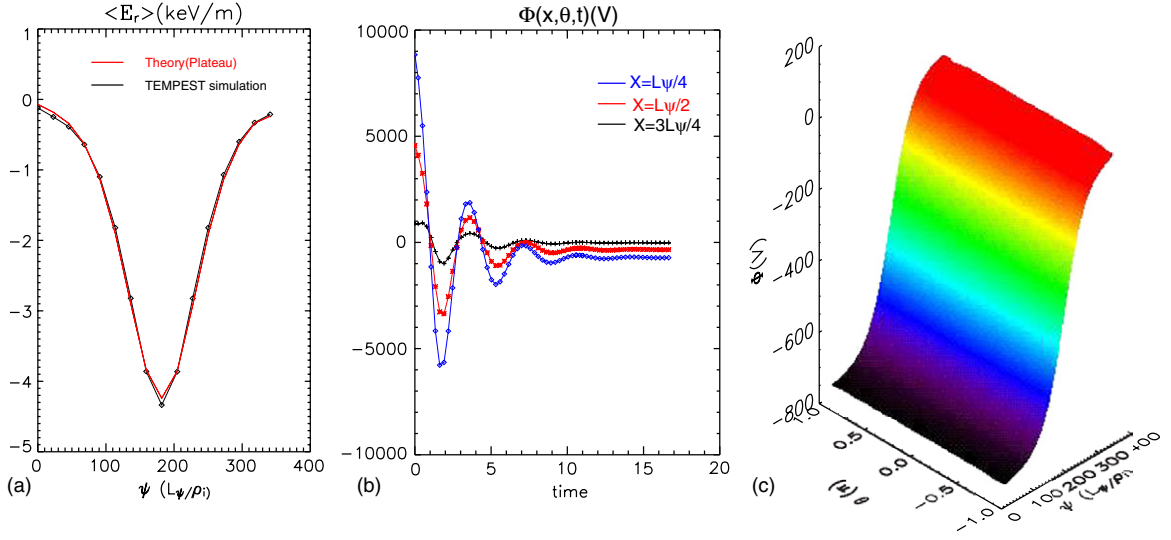


Figure 5. (a) E_r from TEMPEST simulations (black) versus neoclassical theory (red) with finite banana-orbit effect in circular geometry with $q = 3$ and $\epsilon = 0.1$; (b) time evolution of the flux-surface-averaged electrostatic potential at different radial locations; (c) the radial-poloidal profile of the electrostatic potential calculated from a TEMPEST simulation at the end of the simulation.

$n_e = \langle n_i(\psi, \theta, t = 0) \rangle \exp(e\phi/T_e) / \langle \exp(e\phi/T_e) \rangle$, where $\langle \rangle$ represents the flux surface average. This choice of coefficient for the Boltzmann electron model means that there is no cross-field electron transport. Both radial and poloidal boundary conditions are periodic. The first full-f, self-consistent simulation results of collisionless damping of GAMs and zonal flow are plotted in figure 4. Comparison between theory [23, 24] and simulations for the frequency of the GAM is shown in figure 4(a) and damping rate in figure 4(b). The 25% difference between theory and simulation may be due to the theory using an asymptotic $1/q^2$ expansion for large q , while $q = 2.2$ in the simulation is not very large. The large effect of the orbit size on the GAM damping rate is illustrated in figure 4(c). For the same parameters, the damping rate is almost zero if the finite drift orbit effect is ignored. The complete descriptions for TEMPEST simulations of GAM collisionless damping and its relevance to the experiments in edge-plasma pedestal will be presented elsewhere [25].

4.4. 4D neoclassical radial electric field with finite orbits

The simulations presented here are carried out for large-aspect-ratio circular geometry with magnetic field $B_t = 7.5$ T, $R_0 = 45.6$ m, $q = 3$ and $\epsilon = 0.1$. The ion density and temperature profiles are initialized as a hyperbolic tangent (tanh) function of radius centred around the middle of simulation domain (such as, $N(\psi) = n_0 + n_m \tanh((\psi - \psi_m)/\Delta_n)$, where $\psi_m = (\psi_0 + \psi_L)/2$ and $\Delta_n = \delta_n \ln(N(\psi_0)/N(\psi_L))$). The boundary ion distribution is a fixed Maxwellian with $N(\psi_0) = 1 \times 10^{20} \text{ m}^{-3}$, $n_L = N(\psi_L) = 5 \times 10^{19} \text{ m}^{-3}$, $T_i(\psi_0) = 3 \text{ keV}$, and $T_i(\psi_L) = 1.5 \text{ keV}$ during a simulation. The δ_n is a parameter to control the radial scale length. In this simulation $\delta_n = 50.5$. The radial boundary condition for the potential is $\partial\phi(\psi_0)/\partial\psi = \phi(\psi_L) = 0$. The electron model is the Boltzmann model specified in section 4.3. A Krook collision model is used with $v_{ii} = 0.15v_{Ti}/R_0$, $v_{Ti} = \sqrt{2T_i(\psi_0)/M_i}$. The neoclassical radial electric field from

TEMPEST simulations agrees very well with the standard neoclassical expression $\langle U_{i||} \rangle = (cT_i/Z_i e B_p) [k(\partial \ln T_i/\partial r) - (\partial \ln P_i/\partial r) - (Z_i e/T_i)(\partial \langle \Phi \rangle/\partial r)]$ with $k = -0.5$ as shown in figure 5(a) in the plateau regime [27]. The radial electric field is generated due to the neoclassical polarization. A time history of the flux surface averaged electric potential in figure 5(b) shows geodesic acoustic oscillations generated by the initial conditions, which then relax to a near steady state, consistent with the previous studies [10, 26]. Due to ion-ion collisions, the Rosenbluth-Hinton residual as discussed in the previous section is damped, and the neoclassical residual is reached. Figure 5(c) shows the radial-poloidal profile of the electrostatic potential calculated from the TEMPEST simulation at the end of the simulation, indicating a uniform poloidal profile.

5. Summary and conclusions

The recently developed full-f, 5D continuum edge-plasma code TEMPEST utilizes high-order spatial differencing and a high-order finite-volume scheme for velocity space to accurately simulate particle convection and Coulomb collisions. TEMPEST runs in both full divertor geometry for maximum applicability to diverted tokamaks and in circular geometry for benchmarking with analytic theories and existing core gyrokinetic codes. TEMPEST demonstrates expected physics results in 3D and 4D verification tests. The initial runs have been done in 5D. The further improvement and development of the TEMPEST code (and its successor codes) will yield a valuable predictive model for the edge pedestal. This work is focused on a fundamental understanding of relevant physics from first-principles theory and simulations and should greatly increase our confidence in predictions of ITER edge-plasma performance.

Acknowledgments

The authors wish to acknowledge the assistance and encouragement from Drs J.D. Lindl and W.A. Lokke. The

authors thank Drs Alain J. Brizard, L. Chen, A. Dimits, W.D. Dorland, T.S. Hahm, G. Hammett, R.E. Waltz, W.X. Wang and T.-H. Watanabe for fruitful physics discussions. This work was performed under the auspices of the US Department of Energy by the University of California Lawrence Livermore National Laboratory under Contract No W-7405-Eng-48 at LLNL, Grant No DE-FG02-04ER54739 at UCSD and Grants DE-FG03-95ER54309 at general Atomics and DE-AC02-76CHO3073 at PPPL.

Appendix. Fourth-order upwind scheme for nonuniform grid spacing

We write the finite-difference approximation to the first derivative at node i for a discretization of N points as

$$(\partial_\tau f)_i \approx \sum_{j=1}^N a_j(i) f_j. \quad (17)$$

The function value at i is written as $f_i = f(\tau_i)$, where τ_i is defined in section 3.1. For a fourth-order upwind-biased stencil at node i , the support of $\{\tau_{i-3}, \tau_{i-2}, \tau_{i-1}, \tau_i, \tau_{i+1}\}$ leads to the following weights:

$$a_{i+1}(i) = \frac{(\tau_i - \tau_{i-1})(\tau_i - \tau_{i-2})(\tau_i - \tau_{i-3})}{(\tau_{i+1} - \tau_i)(\tau_{i+1} - \tau_{i-1})(\tau_{i+1} - \tau_{i-2})(\tau_{i+1} - \tau_{i-3})}, \quad (18)$$

$$a_i(i) = \frac{1}{(\tau_i - \tau_{i-1})} + \frac{1}{(\tau_i - \tau_{i-2})} + \frac{1}{(\tau_i - \tau_{i-3})} - \frac{1}{(\tau_{i+1} - \tau_i)}, \quad (19)$$

$$a_{i-1}(i) = -\frac{(\tau_{i+1} - \tau_i)(\tau_i - \tau_{i-2})(\tau_i - \tau_{i-3})}{(\tau_{i+1} - \tau_{i-1})(\tau_i - \tau_{i-1})(\tau_{i-1} - \tau_{i-2})(\tau_{i-1} - \tau_{i-3})}, \quad (20)$$

$$a_{i-2}(i) = \frac{(\tau_{i+1} - \tau_i)(\tau_i - \tau_{i-1})(\tau_i - \tau_{i-3})}{(\tau_{i+1} - \tau_{i-2})(\tau_i - \tau_{i-2})(\tau_{i-1} - \tau_{i-2})(\tau_{i-2} - \tau_{i-3})}, \quad (21)$$

$$a_{i-3}(i) = \frac{(\tau_{i+1} - \tau_i)(\tau_i - \tau_{i-1})(\tau_i - \tau_{i-2})}{(\tau_{i+1} - \tau_{i-3})(\tau_i - \tau_{i-3})(\tau_{i-1} - \tau_{i-3})(\tau_{i-2} - \tau_{i-3})}, \quad (22)$$

with $a_j(i) \equiv 0$ otherwise. The formal leading-order truncation error is

$$-\frac{(\tau_{i+1} - \tau_i)(\tau_i - \tau_{i-1})(\tau_i - \tau_{i-2})(\tau_i - \tau_{i-3})}{120} (\partial_\tau^5 f)_i. \quad (23)$$

References

- [1] Brizard A.J. and Hahm T.S. 2007 *Rev. Mod. Phys.* **79** 421
- [2] Qin H., Cohen R.H., Nevins W.M. and Xu X.Q. 2006 *Contrib. Plasma Phys.* **46** 477
Qin H., Cohen R.H., Nevins W.M. and Xu X.Q. 2007 *Phys. Plasmas* **14** 056110
- [3] Hahm T.S. 1996 *Phys. Plasmas* **3** 4658
- [4] Hindmarsh A.C., Brown P.N., Grant K.E., Lee S.L., Serban R., Shumaker D.E. and Woodward C.S. 2005 *ACM Trans. Math. Softw.* **31** 363–96
- [5] Jiang G.S. and Shu C.W. 1996 *J. Comput. Phys.* **126** 202
- [6] Kupfer K. *et al* 1996 *Phys. Plasmas* **3** 3644
- [7] Xiong Z., Cohen R.H., Rognlien T.D. and Xu X.Q. 2007 A high-order finite-volume algorithm for Fokker–Planck collisions in magnetized plasmas *J. Comput. Phys.* submitted
- [8] Dorland W. and Hammett G.W. 1993 *Phys. Fluids B* **5** 812
- [9] Dimits A. and Cohen B.I. 1992 Simulation models for tokamak plasmas *IAEA Technical Committee Meeting (Montreal)*
- [10] Wang W.X. and Hinton F.L. 2001 *Phys. Rev. Lett.* **80** 055002-1
- [11] Dimits A.M. 1993 *Phys. Rev. E* **48** 4070
- [12] Beer M.A., Cowley S.C. and Hammett G.W. 1995 *Phys. Plasmas* **2** 2687
- [13] Scott B. 2001 *Phys. Plasmas* **8** 447
- [14] Falgout R.D., Jones J.E. and Yang U.M. 2006 The design and implementation of hypre, a library of parallel high performance preconditioners *Numerical Solution of Partial Differential Equations on Parallel Computers* ed A.M. Bruaset and A. Tveito vol 51 (Berlin: Springer) pp 267–94
- [15] Hornung R.D. and Kohn S.R. 2002 *Concurrency Comput.: Pract. Exp.* **14** 347–68
- [16] Colella P. *et al* <http://seesar.lbl.gov/anag/chombo/index.html>
- [17] Rognlien T.D. and Cutler T.A. 1980 *Nucl. Fusion* **20** 1003
- [18] Cohen R.H. 1979 *Nucl. Fusion* **19** 1295
- [19] Najmabadi F. *et al* 1994 *Nuc. Fusion* **24** 75
- [20] Cohen R.H. and Xu X.Q. 2007 Progress in kinetic simulation of edge plasmas *Contrib. Plasma Phys.* submitted
- [21] Rosenbluth M.N. and Hinton F.L. 1998 *Phys. Rev. Lett.* **80** 724
- [22] Lebedev V.B. *et al* 1996 *Phys. Plasmas* **3** 3023
- [23] Sugama H. and Watanabe T.H. 2006 *J. Phys. Plasmas* **72** 825–8
- [24] Zhe Gao, Itoh K., Sanuki H. and Dong J.Q. 2006 *Proc. 21st Int. Conf. on Fusion Energy 2006 (Chengdu, 2006)* (Vienna: IAEA) CD-ROM file TH/P2-5 and <http://www-naweb.iaea.org/naweb/physics/FEC/FEC2006/html/index.htm>
- [25] Xu X.Q. *et al* 2007 TEMPEST simulations of collisionless damping of GAM and neoclassical residual in edge plasma pedestal *Phys. Rev. Lett.* submitted
- [26] Novakovskii S.V. *et al* 1997 *Phys. Plasmas* **4** 4272
- [27] Hinton F.L. and Hazeltine R.D. 1976 *Rev. Mod. Phys.* **48** 239